catalysts

MDPI

Article

Highly Dispersed Ni Nanocatalysts Derived from NiMnAl-Hydrotalcites as High-Performing Catalyst for Low-Temperature Syngas Methanation

Bin Lu [1,2], Jiahao Zhuang [1,2], Jinping Du [1], Fangna Gu [1,3,*], Guangwen Xu [4], Ziyi Zhong [5], Qing Liu [6] and Fabing Su [1,3,4,*]

1 State Key Laboratory of Multiphase Complex Systems, Institute of Process Engineering, Chinese Academy of Sciences, Beijing 100190, China; lubin162@mails.ucas.edu.cn (B.L.); zhuangjiahao15@mails.ucas.ac.cn (J.Z.); djp0914@163.com (J.D.)
2 School of Chemical Engineering, University of Chinese Academy of Sciences, Beijing 100049, China
3 Zhongke Langfang Institute of Process Engineering, Fenghua Road No 1, Langfang Economic & Technical Development Zone, Hebei 065001, China
4 Institute of Industrial Chemistry and Energy Technology, School of Chemical Engineering Shenyang University of Chemical Technology, Shenyang, Liaoning 110142, China; gwxu@ipe.ac.cn
5 College of Engineering, Guangdong Technion Iarael Institute of Technology (GTIIT), 243 Daxue Road, Shantou 515063, China; ziyi.zhong@gtiit.edu.cn
6 Key Laboratory of Low Carbon Energy and Chemical Engineering, College of Chemical and Environmental Engineering, Shandong University of Science and Technology, Qingdao 266590, China; qliu@sdust.edu.cn
* Correspondence: fngu@ipe.ac.cn (F.G.); fbsu@ipe.ac.cn (F.S.); Tel.: +86-10-82544850 (F.S.); Fax: +86-10-82544851 (F.G.)

Received: 15 February 2019; Accepted: 7 March 2019; Published: 19 March 2019

Abstract: Increasing the low-temperature performance of nickel-based catalysts in syngas methanation is critical but very challenging, because at low temperatures there is high concentration of CO on the catalyst surface, causing formation of nickel carbonyl with metallic Ni and further catalyst deactivation. Herein, we have prepared highly dispersed Ni nanocatalysts by in situ reduction of NiMnAl-layered double hydroxides (NiMnAl-LDHs) and applied them to syngas methanation. The synthesized Ni nanocatalysts maintained the nanosheet structure of the LDHs, in which Ni particles were decorated with MnO_y species and embedded in the AlO_x nanosheets. It was observed that the Ni nanocatalysts exhibited markedly better low-temperature performance than commercial catalysts in the syngas methanation. At 250 °C, 3.0 MPa and a high weight hourly space velocity (WHSV) of 30,000 $mL \cdot g^{-1} \cdot h^{-1}$, both the CO conversion and the CH_4 selectivity reached 100% over the former, while those over the commercial catalyst were only 14% and 76%, respectively. Furthermore, this NiMnAl catalyst exhibited strong anti-carbon and anti-sintering properties at high temperatures. The enhanced low-temperature performance and high-temperature stability originated from the promotion effect of MnO_y and the embedding effect of AlO_x in the catalyst.

Keywords: low-temperature methanation; nickel carbonyl; NiMnAl-LDHs; Ni nanocatalysts

1. Introduction

Over the last few decades, the preparation of synthetic natural gas (SNG) by coal gasification has attracted worldwide attention, particularly in the coal-rich regions, because of the requirements for efficient utilization of coal resources and for a secure supply of natural gas, which is a clean fuel [1,2]. The main technology of producing SNG from syngas is CO methanation [3–5]. Until now, all commercial methanation catalysts for SNG production have been Ni-based catalysts due to their

high performance and low cost [6–18]. Nevertheless, the major weaknesses of nickel catalysts include agglomeration of Ni nanoparticles, formation of carbon deposits at higher temperatures, and poor activity at low temperatures (250 °C) for the complete methanation of syngas [19–31]. The increase in low temperature performance of the Ni catalysts in syngas methanation is critical. It is also very challenging because the high concentration of CO on the catalyst surface may lead to the formation of $Ni(CO)_4$ and further catalyst deactivation. At present, research on low-temperature methanation is mainly focused on hydrogen-rich systems and slurry-bed reactors [32–37], while that for syngas ($H_2/CO = 3/1$) in fixed beds has rarely been reported.

Layered double hydroxides (LDHs) are widely used as catalysts or supports due to their unique layered structure with distribution of M^{2+} (M = Mg, Co, Cu, Ni) and N^{3+} (N = Al, Fe, Co, Mn) cations that are adjustable both in ratio and in type [38–43]. Ni-based hydrotalcites have been used as precursors to obtain methanation catalysts via high temperature calcination followed by reduction [13,44]. However, high temperature calcination would destroy the layered structure of LDHs and reduce the specific surface area and pores volume, which leads to poor activity of the obtained catalysts at low temperatures [45,46]. He et al. found that the Ni nanocatalysts prepared via in situ reduction of NiAl-hydrotalcites with abundant surface defects showed excellent catalytic performance in CO_2 methanation [47]. Differing from CO_2 methanation, the major challenge for low temperature methanation of high concentration CO is a catalyst deactivation phenomenon due to formation of $Ni(CO)_4$. In general, low temperature and high CO partial pressure favor formation of $Ni(CO)_4$ at equilibrium; thus, the inlet temperature of the feed gas should be above 300 °C for SNG, at which the catalyst can convert part of CO and maintain a low CO partial pressure so that $Ni(CO)_4$ formation is negligible. In principle, the reaction can be operated smoothly at quite low temperatures so that the catalyst can be active enough to maintain a low CO concentration on the catalyst surface. Therefore, developing highly active catalysts for low-temperature CO methanation is possible but quite challenging.

Herein, highly dispersed Ni nanocatalysts were obtained by in situ reduction of NiMnAl-LDHs precursors and applied to CO methanation for the first time. The novel catalysts showed excellent catalytic performance at low temperatures and high stability at high temperatures. According to experimental results, the Ni nanocatalysts decorated with MnO_y species and embedded in the AlO_x nanosheets have the application prospect for low temperature methanation.

2. Results and Discussion

2.1. Structure and Morphology of LDHs and Catalysts

The X-ray diffraction (XRD) results of the $NiMn_xAl_{10}$-LDHs (x = 0, 0.5, 1, 2) are shown in Figure 1a and the inset shows the displacement of the first diffraction peak. The diffraction peaks of all the samples at 2θ = 11.6°–11.9°, 23.4°, 35.1°, 39.6°, 46.8°, 61.2° and 62.5° are corresponding to the (003), (006), (009), (015), (018), (110), and (113) planes of typical hydrotalcites, respectively [41]. Table 1 shows the lattice parameters of the $NiMn_xAl_{10}$-LDHs. The lattice parameter "a" is related to the radius of the cation [48]. Compared with NiAl-LDH, the values of "a" for NiMnAl-LDHs do not change after adding Mn^{2+}, because the ionic radius of Ni and Mn (0.62 Å for Ni^{2+}, 0.66 Å for Mn^{2+}, respectively) are relatively close, while the additive amount of Mn is low. When the Mn/Al molar ratios change from 0:10 to 1:10, the lattice constant "c" gradually increases from 2.255 to 2.286 nm until "c" reaches its maximum value, which is due to the difference in bond strength of Ni-O (372 kJ/mol) and Mn-O (402 kJ/mol). When Ni is substituted by Mn, the bond strength of M-O (M-Metal cation) is increased, resulting in the weakened interaction of the metal cations with the interlayer anions as well as the water molecules, so that the interlayer spacing is increased. These results confirm that most of the added Mn^{2+} entered the layered structure of the hydrotalcites and did not affect crystallinity of LDHs.

The XRD spectrums of the catalysts obtained from reducing LDHs directly are shown in Figure 1b. In comparison to Figure 1a, it can be found that the characteristic peaks of LDHs disappeared after the

reduction, but some new diffraction peaks emerged at 2θ = 44.6°, 51.9°, 76.8°, attributing to (111), (200), (220) crystal planes of face-centered cube (fcc) Ni, respectively. Considering the low content of added Mn^{2+} that is difficult to detect, we mainly focus on the diffraction of nickel species. The weak broad diffraction peaks located at 37.1° and 63.3° are attributing to the (111) and (220) crystal planes of NiO (fcc), respectively [41]. The sizes of Ni particles in these NiAl-C, $NiMn_{0.5}Al_{10}$-C, $NiMn_1Al_{10}$-C, and $NiMn_2Al_{10}$-C catalysts were calculated to be 9.0 ± 0.5, 8.7 ± 0.5, 8.5 ± 0.5 and 8.6 ± 0.5 nm, respectively. This indicates that the adding of Mn has only a slight influence on the size of the Ni particles.

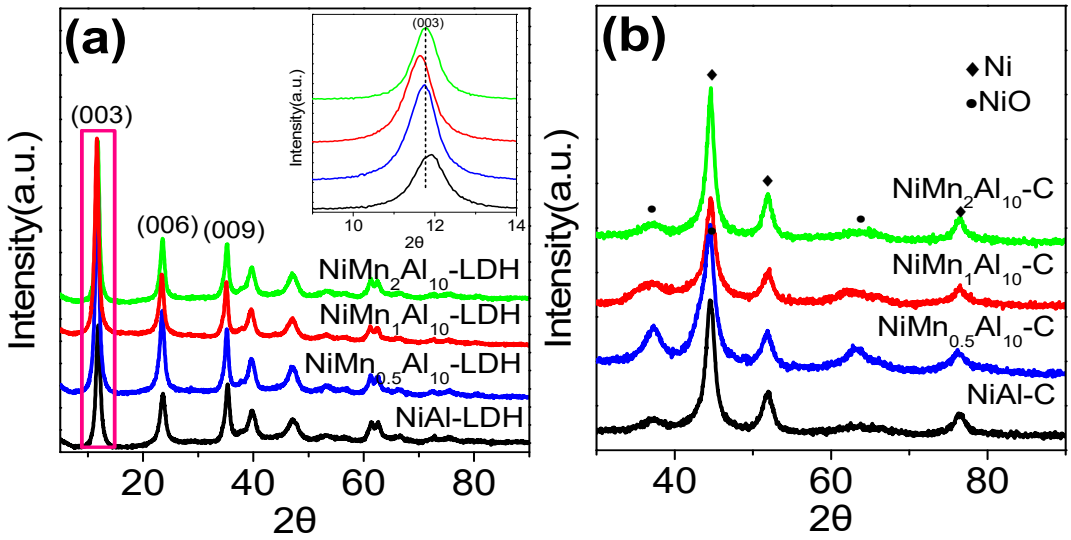

Figure 1. XRD results of LDHs precursors (**a**) and $NiMn_xAl_{10}$ catalysts (**b**). The inset shows the displacement of the first diffraction peak (LDH-layered double hydroxide, C-catalyst).

Table 1. Lattice parameters of the LDHs.

LDHs	d_{003}/nm	d_{006}/nm	d_{009}/nm	d_{110}/nm	[a] $a = 2d_{110}$/nm	[b] $c = (d_{003} + 2d_{006} + 3d_{009})$/nm
NiAl-LDH	0.741	0.378	0.255	0.151	0.302	2.258
$NiMn_{0.5}Al_{10}$-LDH	0.752	0.378	0.255	0.151	0.302	2.269
$NiMn_1Al_{10}$-LDH	0.758	0.378	0.255	0.151	0.302	2.275
$NiMn_2Al_{10}$-LDH	0.752	0.378	0.255	0.151	0.302	2.269

[a] The average distance of the metal cations in the hydrotalcite layer; [b] Three times of the interlayer thickness.

The scanning electron microscope (SEM) images of $NiMn_xAl_{10}$-LDHs before and after the reduction are shown in Figure 2. The hydrothermally synthesized LDHs are composed of the connected nanosheets with relatively uniform size and smooth surface (Figure 2a–d). The $NiMn_xAl_{10}$ catalysts obtained after reduction maintain the flake-like morphology but with a rougher surface (Figure 2e–h). The SEM results demonstrate that the incorporation of Mn has no obvious effect on the morphology of LDHs crystals, and the thin layered structure was still preserved after reduction, which is helpful to investigate the change of Ni particles before and after methanation reaction.

The physical properties of the catalysts were investigated by BET (Figure 3). As can be seen from Figure 3a, all the catalysts exhibit IV type adsorption-desorption isotherms with type H3 hysteresis loops. The specific surface areas of the catalysts are similar (shown in Table 2). Nonetheless, the pore volume of $NiMn_{0.5}Al_{10}$-C and $NiMn_1Al_{10}$-C are relatively larger, which is possibly caused by the formation of macropores from the packing of nanosheets (Figure 3b).

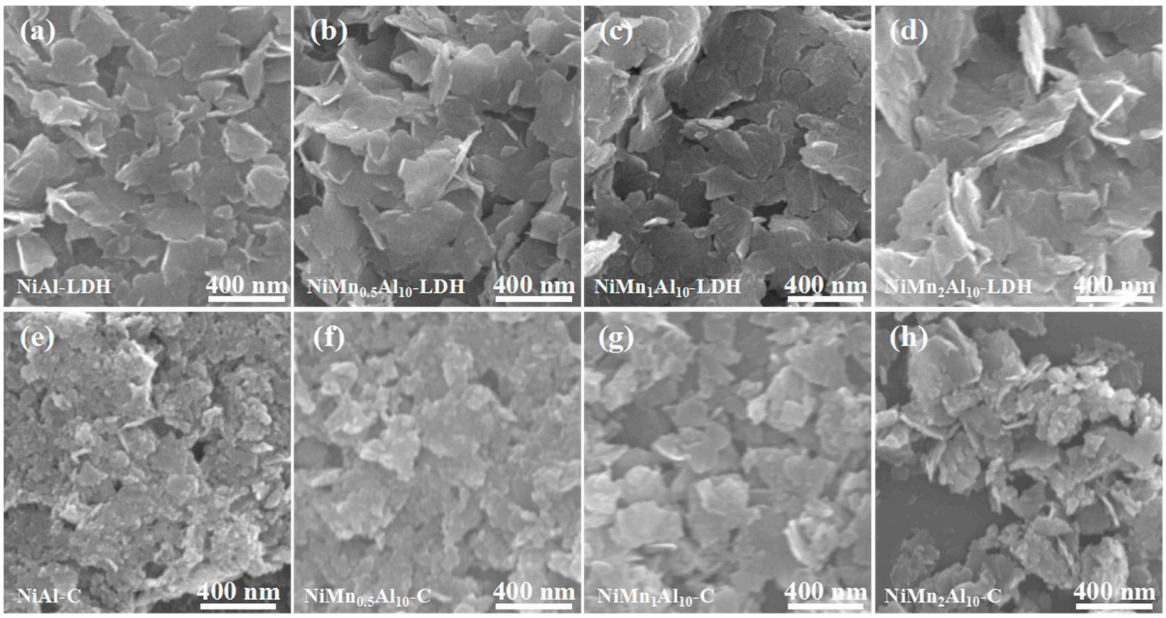

Figure 2. SEM images of the LDHs precursors (**a**–**d**) and the corresponding catalysts after reduction (**e**–**h**).

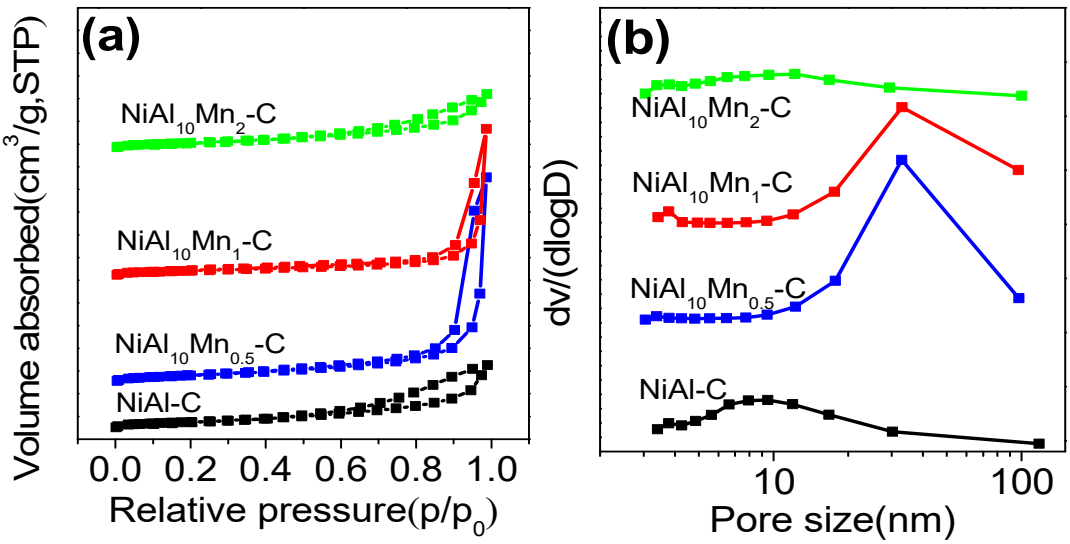

Figure 3. N_2-adsorpotion/desoportion isotherms (**a**) and pore size distribution of catalysts (**b**).

Table 2. Physicochemical property of catalysts.

Catalysts	[a] Wt% ± 0.1			[b] S_{BET} ($m^2 \cdot g^{-1}$)	[c] V_p ($cm^3 \cdot g^{-1}$)	[d] H_2 Uptake (μmoL/g)	[e] De (%) ± 0.1
	Ni	Al	Mn				
NiAl-C	61.7	7.3	0	76	0.2	534	10.2
$NiMn_{0.5}Al_{10}$-C	57.5	7.3	0.6	87	0.5	559	11.4
$NiMn_1Al_{10}$-C	57.8	7.7	1.7	69	0.7	631	12.8
$NiMn_2Al_{10}$-C	57.9	7.9	3.2	66	0.2	550	11.2

[a] Determined by ICP; [b] Calculated by BET equation; [c] Determined by the volume of N_2 adsorbed at $p/p^0 = 0.97$; [d] Calculated based on the H_2-TPD data; [e] Calculated using the H_2-TPR and H_2-TPD results.

The reduction behaviors of LDHs were investigated by H_2-TPR (Figure 4a). All the samples have two distinct reduction peaks: the first one located at 300–450 °C is derived from the reduction of Ni oxide species with a weak interaction with the substrate, and the second one at 450–700 °C is attributed

to the reduction of Ni oxide species, having a strong interaction with the matrix. As the molar ratio of Mn/Al changes from 0:10 to 1:10, the first reduction peak shifts to low temperature range, indicating that adding a proper amount of Mn can improve the reduction of nickel species [12]. However, with further increase of Mn/Al molar ratio to 2:10, the reduction temperature of the catalyst is increased again, because of the reinforced interaction between nickle oxide species and the excess of Mn oxide species [12]. Figure 4b shows the H_2-TPD curves of the $NiMn_xAl_{10}$ catalysts. Although MnO_x is capable of adsorbing hydrogen, the amount of Mn is much lower than that of Ni in the catalyst, so we will mainly focus on the H_2 uptake of Ni. In addition, there is no H_2 uptake of Al_2O_3 [11,24,28]. Therefore, the dispersion of Ni particles can be calculated from the H_2-TPD results. All catalysts have only one H_2 desorption peak at the temperature interval of 100–200 °C, corresponding to desorption of H_2 of highly dispersed Ni nanoparticles or Ni nanoparticles with many surface defects [12], which are benefit to the diffusion and dissociation of surface hydrogen [49]. Table 2 lists the H_2 adsorption amount on a series of $NiMn_xAl_{10}$ (x = 0, 0.5, 1, 2) catalysts. Among them, $NiMn_1Al_{10}$ shows the maximum H_2 uptake of 631 μmol/g_{cat} and highest Ni distribution of 12.8 ± 0.1%, indicating that incorporating an appropriate amount of Mn can significantly improve the H_2 adsorption capacity and the dispersion of Ni nanoparticles. However, excessive Mn will overlay fractional the active site of Ni particles and reduce the adsorption capacity for H_2, which is very important for the performance of the catalyst.

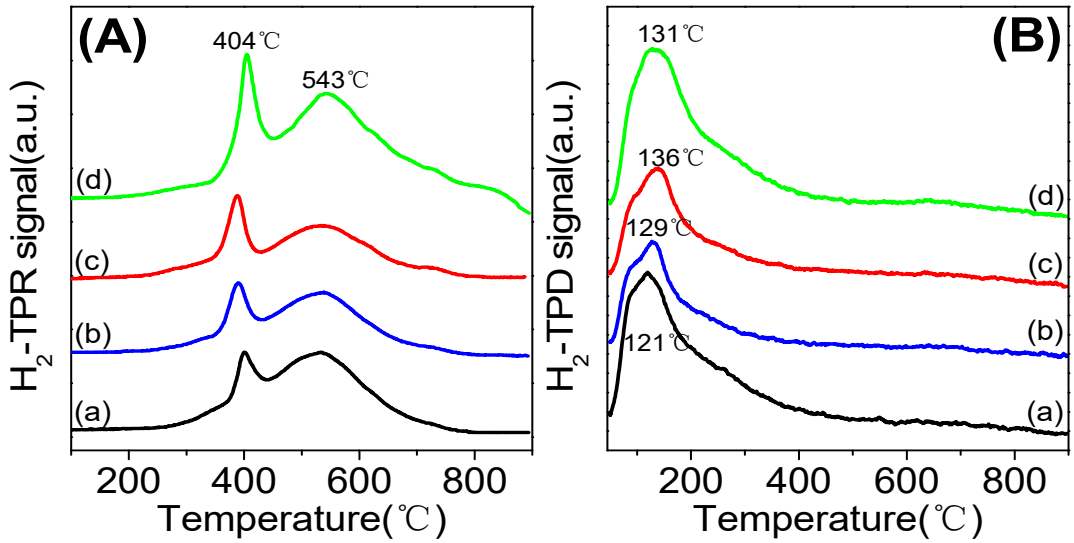

Figure 4. (**A**) H_2-TPR curves of the LDHs: (a) NiAl-LDH, (b) $NiMn_{0.5}Al_{10}$-LDH, (c) $NiMn_1Al_{10}$-LDH, (d) $NiMn_2Al_{10}$-LDH and (**B**) H_2-TPD results of the catalysts: (a) NiAl-C, (b) $NiMn_{0.5}Al_{10}$-C, (c) $NiMn_1Al_{10}$-C and (d) $NiMn_2Al_{10}$-C.

The dispersion of Ni nanoparticles was further investigated by transmission electron microscopy (TEM) (Figure 5). As can be seen from TEM images (Figure 5a–d), the catalysts maintain the nanosheet morphology of the LDHs precursors. Additionally, Ni nanoparticles are highly dispersed and embedded in the AlO_x matrix. The inserted histograms show the size distributions of the Ni nanoparticles. The average diameters of Ni in NiAl-C, $NiMn_{0.5}Al_{10}$-C, $NiMn_1Al_{10}$-C and $NiMn_2Al_{10}$-C are 12.6 ± 0.5, 12.3 ± 0.5, 10.6 ± 0.5 and 12.4 ± 0.5 nm (based on measurements of 150 particles), respectively. These results are very close to those calculated from the XRD results. The lattices and distribution of Ni and Mn species on the substrate can be observed from the high resolution transmission electron microscopy (HRTEM) images. The lattice distance of 0.20, 0.25 and 0.21 nm is attributed to the (111) plane of Ni (fcc) particles, the (211) plane of Mn_3O_4 and the (420) plane of Mn_2O_3, respectively. The reason why Mn exists in the form of oxides is that the reduction order of MnO_y is first from MnO_2/Mn_2O_3 to Mn_3O_4, and then to MnO, and the final reduction to elemental Mn

requires a temperature higher than 800 °C [50]. The TEM image of NiAl-C demonstrates Ni particles are fixed by the poorly crystallized AlO_x shell (Figure 5e), and the AlO_x is formed during the reduction of the LDHs precursors [41]. For the Mn-added catalyst, Ni particles and the adjacent MnO_y are collectively confined in the matrix of AlO_x (Figure 5e), which is critical to improve the stability of the catalyst. The XRD, SEM, and TEM results show that the Mn incorporated LDHs maintains its structural characteristics during in situ reduction, which is beneficial to preparation Ni-based catalysts embedded in AlO_x matrix with high dispersion.

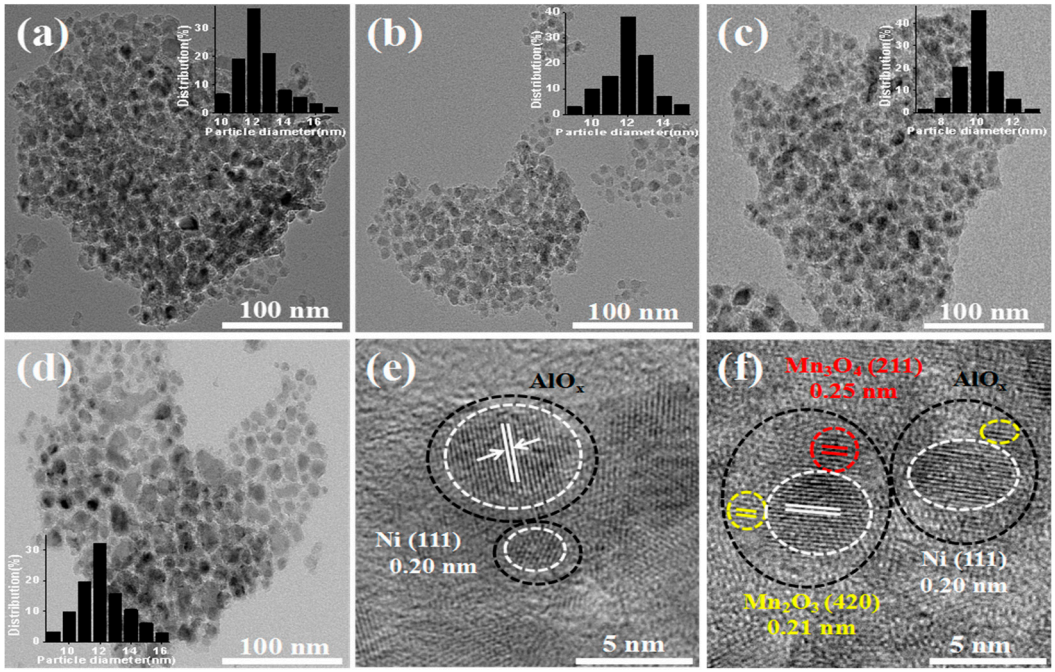

Figure 5. TEM pictures of the catalysts: (**a**–**f**) NiAl-C, $NiMn_{0.5}Al10$-C, $NiMn_1Al_{10}$-C, $NiMn_2Al_{10}$-C, NiAl-C and $NiMn_1Al_{10}$-C. The insets show the size distribution of Ni nanoparticles.

Energy dispersive spectroscopy (EDS) mapping was used to characterize the spatial distribution of individual elements in the catalyst (Figure 6). Fig. 6a shows that the signal of Ni element is strong in the central part of the particles, while the Al and O elements are mainly distributed around Ni particles. The distribution of Mn element cannot be clearly seen in Figure 6a due to the small amount of Mn in the catalyst. The spatial distribution of Ni and Mn in the $NiMn_1Al_{10}$-C catalyst is shown in Fig. 6b. MnO_y (Mn_3O_4 or Mn_2O_3) is also dispersed around the Ni particles; thus, both the AlO_x and MnO_y have a certain steric hindrance effect on the agglomeration of the Ni particles to increase the stability of the catalysts. In addition, it can be seen from Fig. 6b that MnO_y is distributed around the Ni particles, which coincides exactly with the TEM results (Figure 5f).

The surface valence of the catalysts derived from LDHs precursors were investigated by XPS (Figure 7). The Ni $2p_{3/2}$ spectrums are shown in Figure 7A. The surface of all the catalysts is composed of a large portion of Ni^{2+} (855.8 eV), and a little part of Ni^0 (853.1 eV), which is probably due to the samples being exposed to air prior to testing and the surface Ni species being oxidized [14,50]. After adding Mn in the catalyst, the binding energy of Ni $2p_{3/2}$ shifts from 855.6 to 855.9 eV, which can be attributed to the interaction between MnO_y and Ni [51]. The spectrum of Mn $2p_{3/2}$ can be broken up into three peaks with centers at 647.7, 642.9, and 637.8 eV, which are corresponding to the Mn^{4+}, Mn^{3+} and Mn^{2+} species, respectively [12,51–53]. With the increase of Mn content, the Mn^{4+}/Mn^{3+} atomic ratios in the catalysts significantly increased (Figure 7B and Table 3). O_{1s} spectra are shown in Figure 7C. All the catalysts are shown a broad peak that can be fitted into two peaks by searching for the optimal combination of Gaussian bands. The obtained two peaks center at 530.5 eV and 531.8 eV are attributed to lattice oxygen (O_I) and surface adsorbed oxygen (O_{II}), respectively [53,54].

The amounts of oxygen vacancies are positively correlated with the relative percentage of adsorbed oxygen species [50,51]. The integrated area ratios of $O_{II}/(O_{II} + O_I)$ are listed in Table 3, indicating that the incorporated Mn can significantly increase the oxygen vacancies in the catalyst.

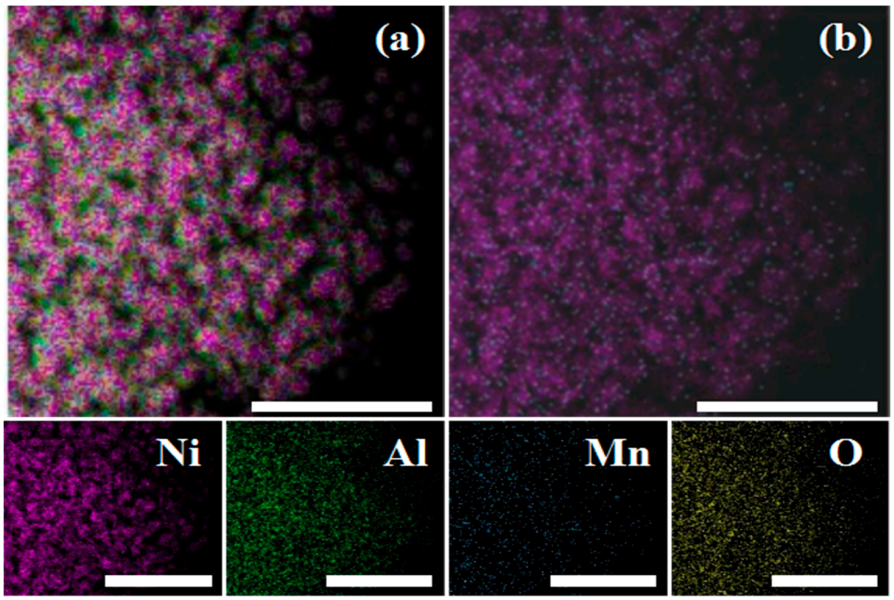

Figure 6. TEM-EDS mapping of the $NiMn_1Al_{10}$-C catalyst: (**a**) overlap of Ni, Al, Mn and O, (**b**) overlap of Ni and Mn. The scale bar is 20 nm.

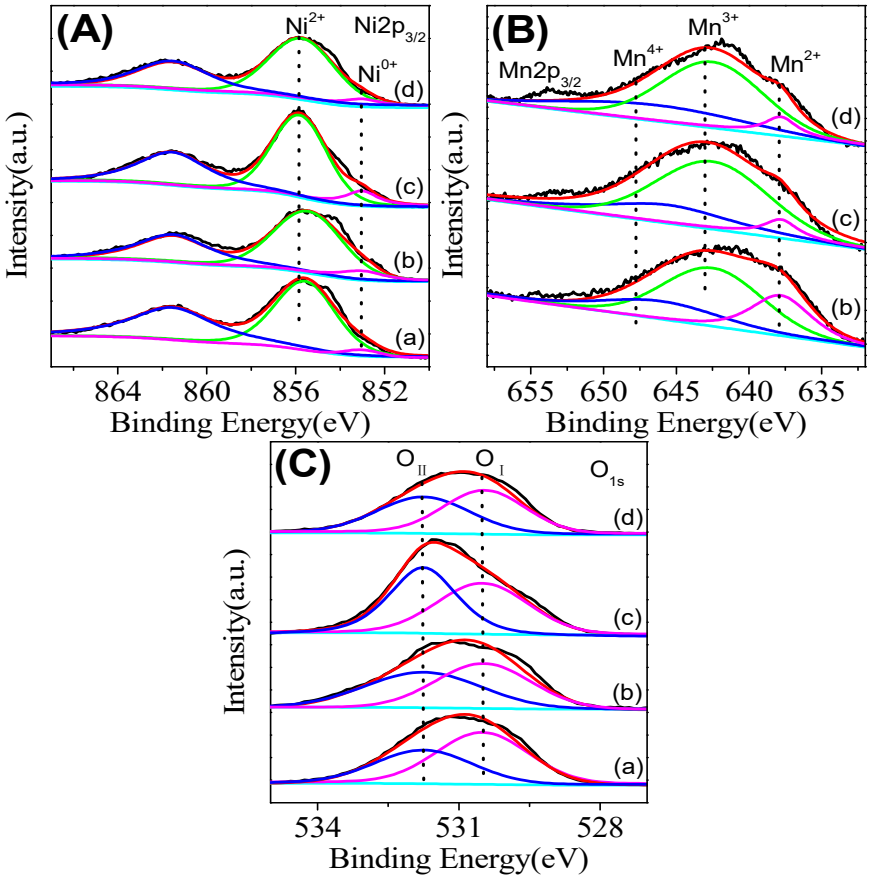

Figure 7. XPS spectras of the catalysts: (**A**) Ni 2p, (**B**) Mn 2p, (**C**) O 1s. (a) NiAl-C, (b) $NiMn_{0.5}Al_{10}$-C, (**C**) $NiMn_1Al_{10}$-C and (d) $NiMn_2Al_{10}$-C.

Table 3. Surface valence of catalysts determined by XPS.

Catalysts	Mn $2p_{2/3}$ Position (eV)			Mn^{4+}/Mn^{3+}	O 1s Position (eV)		$O_{II}/(O_{II} + O_I)$
	Mn^{2+}	Mn^{3+}	Mn^{4+}		O_I	O_{II}	
NiAl-C	-	-	-	-	530.5	531.8	0.41
$NiMn_{0.5}Al_{10}$-C	637.8	642.8	647.7	0.33	530.5	531.8	0.49
$NiMn_1Al_{10}$-C	637.9	642.9	647.6	0.59	530.5	531.8	0.56
$NiMn_2Al_{10}$-C	637.9	643.0	647.8	0.48	530.4	531.7	0.50

Based on the above results, it is found that both MnO_y and Ni particles are fixed by the AlO_x matrix, and MnO_y is distributed around the Ni particles. In order to further elaborate the microstructure of the catalyst, we have drawn a schematic diagram of the structure of the catalyst (Figure 8). During the reduction process, the layered structure of LDHs is collapsed to form Ni(MnAl)O_x nanosheets, and the Ni clusters decorated with MnO_y species are formed, half-buried, and distributed on the nanosheets. In other words, the Ni particles are decorated with MnO_y and embedded on the AlO_x matrix [41]. The segregation effect of the AlO_x matrix prevents the sintering of Ni particles during the methanation reaction, thereby increasing the service life of the catalyst. In summary, the nickel-based catalyst synthesized by in situ reduction of LDHs has a unique structure, which is important for enhancing the low temperature activity and high temperature stability of the catalyst.

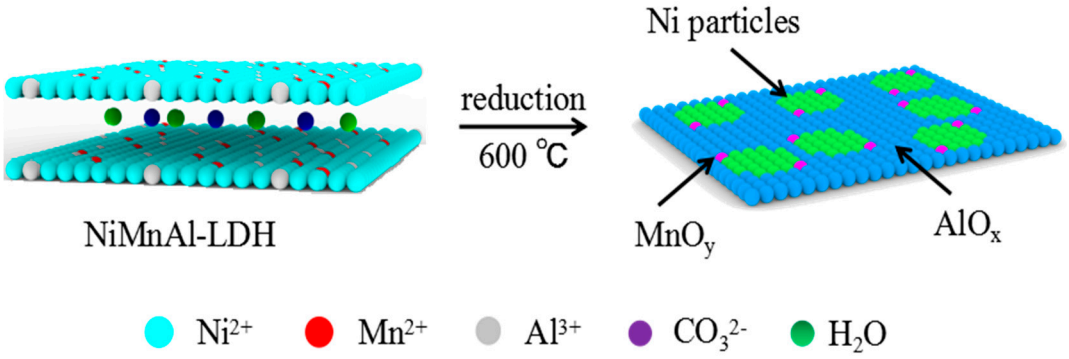

Figure 8. Schematic diagram of the structure of the catalyst.

2.2. Catalytic Activity

Generally, high pressure is used in the synthesis of SNG in the industry [14]. For the purpose of studying the low temperature activity of the catalysts for CO methanation under the industrial reaction conditions, the performance test was executed at 3.0 MPa and a WHSV of 30,000 $mL \cdot g^{-1} \cdot h^{-1}$ (Figure 9). For NiAl-C, the CO conversion and CH_4 yield at 250 °C is 62% and 59%, respectively. After adding Mn in the catalyst, the performances of $NiMn_xAl_{10}$-C are significantly improved (shown in Figure 9a–b). Among them, $NiMn_1Al_{10}$-C exhibits the highest performance at low temperature, and both CO conversion and selectivity of CH_4 achieve 100% at 250 °C, owning to the high scatter of Ni nanoparticles and H_2 uptake (Table 2), and appearance of a number of oxygen vacancies in the catalyst (Table 3). However, the conversion of CO on commercial catalyst (Ni-35.3 wt%) is only 14% at the same reaction condition. To the best of our knowledge, there is no reported Ni-based catalyst that can achieve 100% conversion of CO at such low temperatures and high pressure of CO with feed gas H_2:CO of 3:1 [16,24,26], at which the conventional nickel-based catalysts are susceptible to inactivation owing to the formation of $Ni(CO)_4$. In this work, the synthesized $NiMn_xAl_{10}$-C can convert most of the CO even at low temperatures, so that the CO concentration on the surface of the catalysts is very low, which can avoid the formation of nickel carbonyl. Therefore, the $NiMn_xAl_{10}$-C catalyst is promising in industrial applications of low temperature methanation.

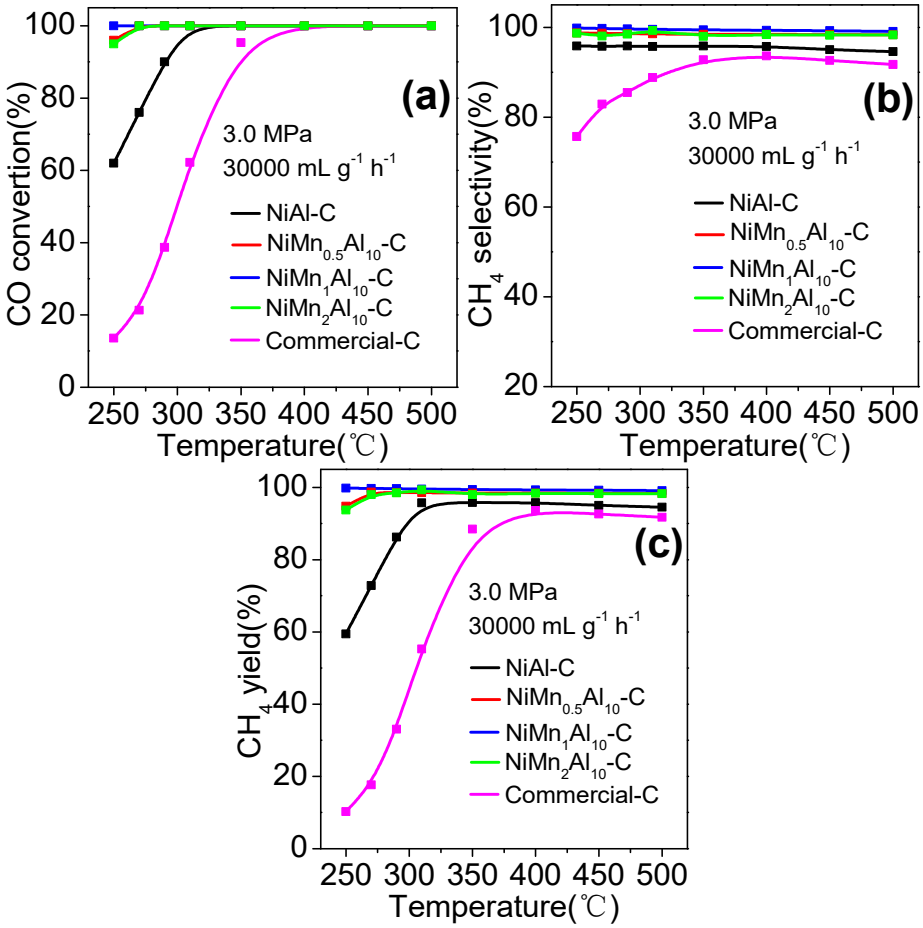

Figure 9. Catalytic activity of the catalysts for CO methanation: (**a**) CO conversion, (**b**) CH_4 selectivity, (**c**) CH_4 yield.

The durability test is indispensable for further investigation of the low temperature performance of the catalysts (Figure 10a). The conversion of CO of the Commercial-C decreased from 36% to 24% after 23 h of reaction at a low temperature. The amount of Ni of the fresh and used catalysts are determined by ICP; we found that the amount of Ni decreased from 35.3 wt% to 28.4 wt%, which is a result of the formation of a $Ni(CO)_4$. However, the performance of the $NiMn_1Al_{10}$-C did not decrease, which was attributed to the fact that the added Mn increased the H_2 uptake and the number of oxygen vacancies (Figures 4b and 7C). Although Commercial-C has poor low temperature activity, its high temperature stability is good [9]. Furthermore, a good methanation catalyst should show high performance at low temperatures and strong resistance against sintering and coking at high temperatures. Therefore, the stability of $NiMn_1Al_{10}$-C was evaluated at 500 °C and 3.0 MPa with different space velocities. The $NiMn_1Al_{10}$-C is very stable at a high temperature with different space velocities: the CO conversion maintains at 100% for 180 h, and the selectivity of CH_4 is slightly reduced when the space velocity is increased from 30,000 $mL \cdot g^{-1} \cdot h^{-1}$ to 60,000 $mL \cdot g^{-1} \cdot h^{-1}$(Figure 10b). Compared with the supported nickel-based catalyst, the $NiMn_XAl_{10}$-C catalyst has high low-temperature activity and strong anti-sintering performance [15,17,35,37]. The high stability of the $NiMn_1Al_{10}$-C at high temperatures is attributed to the confinement effect of AlO_x and MnO_y (Figures 5f and 6), which prevents the sintering of Ni particles during the reaction.

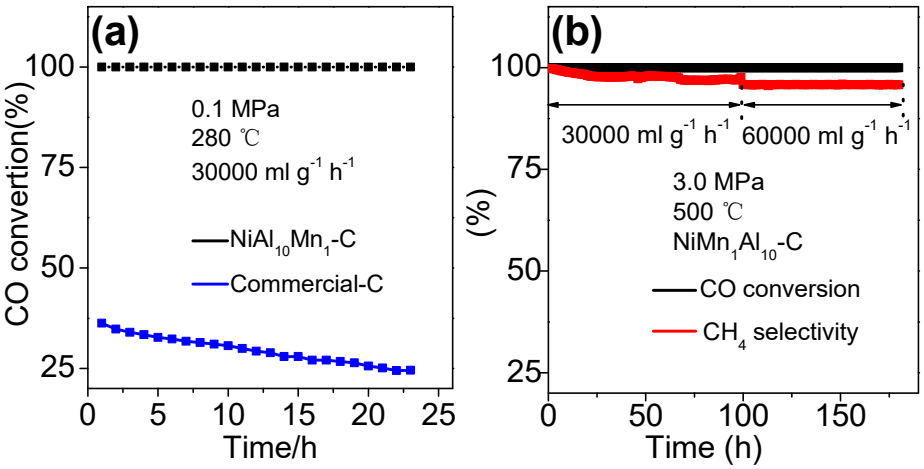

Figure 10. Low temperature (**a**) and high temperature (**b**) lifetime tests of the catalysts.

The XRD results of the fresh and used $NiMn_1Al_{10}$-C are shown in Figure 11a, and both of them display the characteristic peaks at 2θ = 44.6°, 51.9°, 76.8°, attributing to (111), (200), (220) planes of Ni (fcc), respectively. Additionally, the peak intensities of Ni for the used catalyst almost do not change compared with that of the fresh one. The average diameters of Ni particles in the fresh and used catalysts are 8.5 ± 0.5 and 8.3 ± 0.5 nm, respectively, indicating there was no agglomeration of the Ni particles after the high temperature stability test. The result proves that the $NiMn_1Al_{10}$-C catalyst has a high stability at high temperatures, which was due to the confinement of the AlO_x substrate (Figure 5). The carbon deposit amount was investigated by thermogravimetric (TG) (Figure 11b). The weights of fresh and used catalysts increased at 200–400 °C is associated with the oxidation of the reduced Ni particles. The superposition of both TG curves indicates that there were almost no carbon deposits formed, implying that $NiMn_1Al_{10}$-C possesses excellent anti-coking properties due to the high H_2 adsorption and catalyst containing a larger number of oxygen vacancies (Tables 2 and 3). By contrast, with the nickel-based catalyst synthesized by traditional means [9–11,15,21], the $NiMn_1Al_{10}$-C catalyst exhibits much higher stability due to greatly improved resistance to coking and sintering. The carbon deposit amount was further investigated by Raman spectra (Figure 11c). No peak of carbon was observed, indicating that there was no carbon deposit on the used catalyst surface.

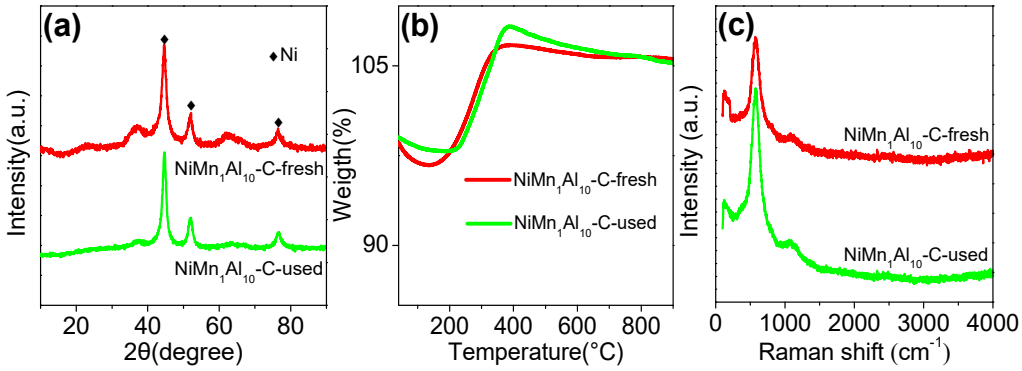

Figure 11. XRD (**a**), TG (**b**) and Raman spectrum (**c**) of the catalysts.

3. Materials and Methods

3.1. Chemicals

Aluminum nitrate nonahydrate ($Al(NO_3)_3{\cdot}9H_2O$), urea ($CO(NH_2)_2$), Nickel (II) nitrate hexahydrate ($Ni(NO_3)_2{\cdot}6H_2O$) and manganese nitrate ($Mn(NO_3)_2{\cdot}4H_2O$) were purchased from

Sinopharm Chemical Reagent Co. Ltd., Shanghai, China. All reagents were of analytical grade and used without further purification.

3.2. Catalysts Preparation

The NiAl hydrotalcite was prepared by hydrothermal method. First, 1.5 mmol of $Ni(NO_3)_2{\cdot}6H_2O$, 0.5 mmol of $Al(NO_3)_3{\cdot}9H_2O$ and 10 mmol of $CO(NH_2)_2$ were dissolved in 70 mL of deionized water. Then the solution was transferred into an autoclave for a hydrothermal treatment at 120 °C for 12 h. Subsequently, the product was centrifuged and washed with deionized water. The collected product was subsequently dried at 80 °C for 15 h, which was named NiAl-LDH. The synthesis of the NiMnAl ternary hydrotalcites is similar to the above process, except that a certain amount of $Mn(NO_3)_2{\cdot}4H_2O$ was added. The synthesized NiMnAl ternary hydrotalcites with the molar ratios of Mn/Al (Mn:Al = 0.5:10, 1:10, 2:10) are denoted as $NiMn_{0.5}Al_{10}$-LDH, $NiMn_1Al_{10}$-LDH, and $NiMn_2Al_{10}$-LDH, respectively. After reduction in hydrogen at 600 °C for 2 h (10 °C/min), the methanation catalysts are marked as NiAl-C (C stands for the catalyst), $NiMn_{0.5}Al_{10}$-C, $NiMn_1Al_{10}$-C, and $NiMn_2Al_{10}$-C accordingly. The commercial catalyst (Ni-35.3 wt%) was purchased from LiaoNing HaiTai SCI-TECH Development CO., Ltd., Fushun, China. For comparison with the commercial catalyst, nickel content of the NiMnAl catalysts was diluted to 35 wt% with α-Al_2O_3 (commercial γ-Al_2O_3 (GongYi HuaYu, Zhengzhou, China) calcined at 1200 °C in air for 6 h), and the α-Al_2O_3 is inactive for CO methanation.

3.3. Catalysts Characterization

The X-ray diffraction (XRD) characterization was carried out on Cu-Ka radiation with a rate of 10° min^{-1} (40 kV, 40 mA). N_2 adsorption/desorption isotherms and the specific surface area and pore size distributions of the samples were tested on the Quantachrome NOVA 3200e (FL, USA). The morphology and microscopic feature of the samples were detected by scanning electron microscope (SEM) (JSM-7001F, INCA X-MAX, Tokyo, Japan, 15 kV) and transmission electron microscopy (TEM) (JEM-2010F, JEOL, Tokyo, Japan). Hydrogen temperature programmed reduction (H_2-TPR) and Hydrogen temperature programmed desorption (H_2-TPD) were obtained from Quantachrome automated chemisorption analyzer. In a typical experiment of H_2-TPR, the hydrotalcite precursor (30 mg) was sealed in the quartz U-tube reactor and purged in a He flow for 2 h at 150 °C (10 °C/min), and then reduced by injecting H_2 and Ar (10% H_2/Ar) at a given temperature. In a typical experiment of H_2-TPD, the hydrotalcite precursor (100 mg) firstly in situ reduced with pure H_2, then cooled down in the N_2 atmosphere, and subsequently switched to Ar flow purging for 1.5 h to remove the physically adsorbed H_2 on the surface of the catalysts. The H_2 adsorption amounts of the catalysts were measured at a heating rate of 10 °C/min. The dispersion of Ni nanoparticles was calculated from the data of H_2-TPD, and the calculation details can be found in our previous work [9]. The elements amount of the catalysts were obtained from Optima 7000 DV inductively coupled plasma optical emission spectrometer (ICP, MA, USA). The surface chemical compositions of the catalysts were measured by X-ray photoelectron spectroscopy (XPS) on an Esca Lab 250Xi with a monochromatic Al Kα radiation. The carbon deposits on the surface of the used catalyst were determined by thermogravimetric analyzer (TG/DTA 6300, Seiko Instruments, Tokyo, Japan) and Raman Spectrometer (Renishaw RM 2000, laser wavelength = 532 nm, London, UK).

3.4. Catalytic Performance Measurement

The methanation measurements are similar to what we have reported previously [11]. The CO methanation reaction was performed in a fixed bed reactor at 3.0 MPa, and the reaction data were recorded in the temperature interval of 250–500 °C; the spacing is 20 °C or 50 °C. In each case, the catalyst (200 mg) admixed with 5 g of quartz sand, then heated to the reaction temperature (250 °C) in a H_2 atmosphere, and finally switched to syngas (H_2:CO:N_2 = 3:1:1) for methanation reaction. The mixed gas after the methanation reaction was first cooled down and then analyzed on line by

Micro Gas chromatography (3000A; Agilent Technologies, CA, USA). The amount of H_2, N_2, CH_4, and CO in the outlet gases were analyzed by a thermal conductivity detector (TCD, CA, USA) connected to a molecular sieve column. The amount of CO_2, C_2H_4 and C_2H_6 in the outlet gases were detected by TCD connected to a Plot Q column (CA, USA). The stability of the catalyst is investigated at 3.0 MPa and 500 °C.

4. Conclusions

In summary, to enhance the low-temperature performance of the Ni catalysts for syngas methanation, the highly dispersed Ni nanocatalysts are successfully prepared by in situ reduction of NiMnAl-LDHs precursors, and Ni particles decorated with the promoter of MnO_y are confined in the matrix of AlO_x. The synthesized NiMnAl catalysts exhibit higher properties than the NiAl catalyst since the addition of Mn increases dispersion of Ni particles and H_2 uptake. The $NiMn_1Al_{10}$ exhibits the best performance at low temperatures and the greatest resistance to sintering and coking due to the highest dispersion of Ni and the steric hindrance of AlO_x and MnO_y against aggregation of the Ni particles. This work demonstrates how to enhance the performance of the Ni catalysts in methanation by carefully adding promoter MnO_y and by embedding the fine Ni particles on the AlO_x nanosheets.

Author Contributions: Conceptualization, B.L., F.G. and F.S.; methodology, B.L. and F.G.; validation, B.L., J.Z., J.D., F.G., G.X., Z.Z., Q.L. and F.S.; investigation, B.L. and F.G.; resources, F.G. and F.S.; writing—original draft preparation, B.L., J.Z., J.D., F.G. and F.S.; writing—review and editing, B.L., F.G., G.X., Z.Z., Q.L. and F.S.; supervision, F.G. and F.S.; funding acquisition, F.G. and F.S.

Funding: This research was funded by National Key R&D Program of China (2018YFB0604501) and the National Natural Science Foundation of China (21776286).

Conflicts of Interest: There are no conflicts of interest to declare.

References

1. Razzaq, R.; Li, C.; Zhang, S. Coke oven gas: Availability, properties, purification, and utilization in China. *Fuel* **2013**, *113*, 287–299. [CrossRef]
2. Zhang, J.; Xin, Z.; Meng, X.; Tao, M. Synthesis, characterization and properties of anti-sintering nickel incorporated MCM-41 methanation catalysts. *Fuel* **2013**, *109*, 693–701. [CrossRef]
3. Höhlein, B.; Menzer, R.; Range, J. High Temperature Methanation in the Long-distance Nuclear energy transport system. *Appl. Catal.* **1981**, *1*, 125–139. [CrossRef]
4. Höhlein, B.; Niessen, J.; Schiebahn, H.J.R.; Vorwerk, M. Methane from synthesis gas and operation of high-temperature methanation. *Nucl. Eng. Des.* **1984**, *78*, 241–250. [CrossRef]
5. Nguyen, T.T.M.; Wissing, L.; Skjøth-Rasmussen, M.S. High temperature methanation: Catalyst considerations. *Catal. Today* **2013**, *215*, 233–238. [CrossRef]
6. Ma, S.; Tan, Y.; Han, Y. Methanation of syngas over coral reef-like Ni/Al_2O_3 catalysts. *J. Nat. Gas. Chem.* **2011**, *20*, 435–440. [CrossRef]
7. Zhang, M.; Yu, F.; Li, J.; Chen, K.; Yao, Y.; Li, P.; Zhu, M.; Shi, Y.; Wang, Q.; Guo, X. High CO Methanation Performance of Two-Dimensional Ni/MgAl Layered Double Oxide with Enhanced Oxygen Vacancies via Flash Nanoprecipitation. *Catalysts* **2018**, *8*, 363. [CrossRef]
8. Hu, D.; Gao, J.; Ping, Y.; Jia, L.; Gunawan, P.; Zhong, Z.; Xu, G.; Gu, F.; Su, F. Enhanced Investigation of CO Methanation over Ni/Al_2O_3Catalysts for Synthetic Natural Gas Production. *Ind. Eng. Chem. Res.* **2012**, *51*, 4875–4886. [CrossRef]
9. Liu, Q.; Gao, J.; Zhang, M.; Li, H.; Gu, F.; Xu, G.; Zhong, Z.; Su, F. Highly active and stable Ni/γ-Al_2O_3 catalysts selectively deposited with CeO_2 for CO methanation. *RSC Adv.* **2014**, *4*, 16094–16103. [CrossRef]
10. Liu, Q.; Gu, F.; Zhong, Z.; Xu, G.; Su, F. Anti-sintering ZrO_2-modified Ni/α-Al_2O_3 catalyst for CO methanation. *RSC Adv.* **2016**, *6*, 20979–20986. [CrossRef]
11. Liu, Q.; Gao, J.; Gu, F.; Lu, X.; Liu, Y.; Li, H.; Zhong, Z.; Liu, B.; Xu, G.; Su, F. One-pot synthesis of ordered mesoporous Ni–V–Al catalysts for CO methanation. *J. Catal.* **2015**, *326*, 127–138. [CrossRef]

12. Lu, X.; Gu, F.; Liu, Q.; Gao, J.; Jia, L.; Xu, G.; Zhong, Z.; Su, F. Ni-MnO_x Catalysts Supported on Al_2O_3-Modified Si Waste with Outstanding CO Methanation Catalytic Performance. *Ind. Eng. Chem. Res.* **2015**, *54*, 12516–12524. [CrossRef]
13. Tang, H.; Li, S.; Gong, D.; Guan, Y.; Liu, Y. Bimetallic Ni-Fe catalysts derived from layered double hydroxides for CO methanation from syngas. *Front. Chem. Sci. Eng.* **2017**, *11*, 613–623. [CrossRef]
14. Gao, J.; Jia, C.; Li, J.; Gu, F.; Xu, G.; Zhong, Z.; Su, F. Nickel Catalysts Supported on Barium Hexaaluminate for Enhanced CO Methanation. *Ind. Eng. Chem. Res.* **2012**, *51*, 10345–10353. [CrossRef]
15. Gao, J.; Jia, C.; Zhang, M.; Gu, F.; Xu, G.; Zhong, Z.; Su, F. Template preparation of high-surface-area barium hexaaluminate as nickel catalyst support for improved CO methanation. *RSC Adv.* **2013**, *3*, 18156. [CrossRef]
16. Jia, C.; Gao, J.; Li, J.; Gu, F.; Xu, G.; Zhong, Z.; Su, F. Nickel catalysts supported on calcium titanate for enhanced CO methanation. *Catal. Sci. Technol.* **2013**, *3*, 490–499. [CrossRef]
17. Jin, G.; Gu, F.; Liu, Q.; Wang, X.; Jia, L.; Xu, G.; Zhong, Z.; Su, F. Highly stable Ni/SiC catalyst modified by Al_2O_3 for CO methanation reaction. *RSC Adv.* **2016**, *6*, 9631–9639. [CrossRef]
18. Sun, J.; Feng, Q.; Liu, Q.; Ji, S.; Fang, Y.; Peng, X.; Wang, Z.-J. An Al_2O_3-Coated SiC-Supported Ni Catalyst with Enhanced Activity and Improved Stability for Production of Synthetic Natural Gas. *Ind. Eng. Chem. Res.* **2018**, *57*, 14899–14909. [CrossRef]
19. Wang, X.; Liu, Q.; Jiang, J.-X.; Jin, G.; Li, H.; Gu, F.; Xu, G.; Zhong, Z.; Su, F. SiO_2-stabilized Ni/t-ZrO_2 catalysts with ordered mesopores: One-pot synthesis and their superior catalytic performance in CO methanation. *Catal. Sci. Technol.* **2016**, *6*, 3529–3543. [CrossRef]
20. Jiang, Y.; Huang, T.; Dong, L.; Su, T.; Li, B.; Luo, X.; Xie, X.; Qin, Z.; Xu, C.; Ji, H. Mn Modified Ni/Bsentonite for CO_2 Methanation. *Catalysts* **2018**, *8*, 646. [CrossRef]
21. Feng, F.; Song, G.; Xiao, J.; Shen, L.; Pisupati, S.V. Carbon deposition on Ni-based catalyst with TiO_2 as additive during the syngas methanation process in a fluidized bed reactor. *Fuel* **2019**, *235*, 85–91. [CrossRef]
22. Dai, X.; Liang, J.; Ma, D.; Zhang, X.; Zhao, H.; Zhao, B.; Guo, Z.; Kleitz, F.; Qiao, S. Large-pore mesoporous RuNi-doped TiO_2–Al_2O_3 nanocomposites for highly efficient selective CO methanation in hydrogen-rich reformate gases. *Appl. Catal. B-Environ.* **2015**, *165*, 752–762. [CrossRef]
23. Mebrahtu, C.; Krebs, F.; Perathoner, S.; Abate, S.; Centi, G.; Palkovits, R. Hydrotalcite based Ni-Fe/(Mg, Al)O_x catalysts for CO_2 methanation-tailoring Fe content for improved CO dissociation, basicity, and particle size. *Catal. Sci. Technol.* **2018**, *8*, 1016–1027. [CrossRef]
24. Liu, Q.; Gu, F.; Gao, J.; Li, H.; Xu, G.; Su, F. Coking-resistant Ni-ZrO_2/Al_2O_3 catalyst for CO methanation. *J. Energy. Chem.* **2014**, *23*, 761–770. [CrossRef]
25. Zeng, Y.; Ma, H.; Zhang, H.; Ying, W.; Fang, D. Ni-Ce-Al composite oxide catalysts synthesized by solution combustion method: Enhanced catalytic activity for CO methanation. *Fuel* **2015**, *162*, 16–22. [CrossRef]
26. Zhao, A.; Ying, W.; Zhang, H.; Ma, H.; Fang, D. Ni-Al_2O_3 catalysts prepared by solution combustion method for syngas methanation. *Catal. Commun.* **2012**, *17*, 34–38. [CrossRef]
27. Bian, L.; Zhang, L.; Zhu, Z.; Li, Z. Methanation of carbon oxides on Ni/Ce/SBA-15 pretreated with dielectric barrier discharge plasma. *Mol. Catal.* **2018**, *446*, 131–139. [CrossRef]
28. Liu, Q.; Zhong, Z.; Gu, F.; Wang, X.; Lu, X.; Li, H.; Xu, G.; Su, F. CO methanation on ordered mesoporous Ni-Cr-Al catalysts: Effects of the catalyst structure and Cr promoter on the catalytic properties. *J. Catal.* **2016**, *337*, 221–232. [CrossRef]
29. Liu, Q.; Qiao, Y.; Tian, Y.; Gu, F.; Zhong, Z.; Su, F. Ordered Mesoporous Ni-Fe-Al Catalysts for CO Methanation with Enhanced Activity and Resistance to Deactivation. *Ind. Eng. Chem. Res.* **2017**, *56*, 9809–9820. [CrossRef]
30. Xu, L.; Lian, X.; Chen, M.; Cui, Y.; Wang, F.; Li, W.; Huang, B. CO_2 methanation over Co-Ni bimetal-doped ordered mesoporous Al_2O_3 catalysts with enhanced low-temperature activities. *Int. J. Hydrog. Energy* **2018**, *43*, 17172–17184. [CrossRef]
31. Liu, Q.; Wang, S.; Zhao, G.; Yang, H.; Yuan, M.; An, X.; Zhou, H.; Qiao, Y.; Tian, Y. CO_2 methanation over ordered mesoporous NiRu-doped CaO-Al_2O_3 nanocomposites with enhanced catalytic performance. *Int. J. Hydrog. Energy* **2018**, *43*, 239–250. [CrossRef]
32. Hayashi, K.; Miyao, T.; Tabira, Y.; Higashiyama, K. Low-temperature Selective CO Methanation over Unsupported Nickel Catalyst Covered by Silica Thin Layer. *J. Jpn. Petrol. Inst.* **2016**, *59*, 65–71. [CrossRef]
33. Feng, X.; Dong, C.; Ping, D.; Geng, J.; Zhang, J.; Dong, X. Zr-Modified SBA-15 Supported Ni Catalysts with Excellent Catalytic Performance of CO Selective Methanation in H_2-Rich Fuels. *Catal. Lett.* **2018**, *148*, 2967–2973. [CrossRef]

34. Meng, F.; Song, Y.; Li, X.; Cheng, Y.; Li, Z. Catalytic methanation performance in a low-temperature slurry-bed reactor over Ni-ZrO_2 catalyst: effect of the preparation method. *J. Sol-Gel. Sci. Technol.* **2016**, *80*, 759–768. [CrossRef]
35. Cui, D.; Liu, J.; Yu, J.; Su, F.; Xu, G. Attrition-resistant Ni-Mg/SiO_2-Al_2O_3 catalysts with different silica sources for fluidized bed syngas methanation. *Int J Hydrog. Energy* **2017**, *42*, 4987–4997. [CrossRef]
36. Meng, F.; Li, Z.; Ji, F.; Li, M. Effect of ZrO_2 on catalyst structure and catalytic methanation performance over Ni-based catalyst in slurry-bed reactor. *Int. J. Hydrog. Energy* **2015**, *40*, 8833–8843. [CrossRef]
37. Liu, C.; Zhou, J.; Ma, H.; Qian, W.; Zhang, H.; Ying, W. Antisintering and High-Activity Ni Catalyst Supported on Mesoporous Silica Incorporated by Ce/Zr for CO Methanation. *Ind. Eng. Chem. Res.* **2018**, *57*, 14406–14416. [CrossRef]
38. Chen, G.; Gao, R.; Zhao, Y.; Li, Z.; Waterhouse, G.I.N.; Shi, R.; Zhao, J.; Zhang, M.; Shang, L.; Sheng, G.; et al. Alumina-Supported CoFe Alloy Catalysts Derived from Layered-Double-Hydroxide Nanosheets for Efficient Photothermal CO_2 Hydrogenation to Hydrocarbons. *Adv. Mater.* **2018**, *30*. [CrossRef]
39. Chen, G.; Wang, T.; Zhang, J.; Liu, P.; Sun, H.; Zhuang, X.; Chen, M.; Feng, X. Accelerated Hydrogen Evolution Kinetics on NiFe-Layered Double Hydroxide Electrocatalysts by Tailoring Water Dissociation Active Sites. *Adv. Mater.* **2018**, *30*. [CrossRef]
40. Li, P.; Zhu, M.; Tian, Z.; Han, Y.; Zhang, Y.; Zhou, T.; Kang, L.; Dan, J.; Guo, X.; Yu, F.; et al. Two-Dimensional Layered Double Hydroxide Derived from Vermiculite Waste Water Supported Highly Dispersed Ni Nanoparticles for CO Methanation. *Catalysts* **2017**, *7*, 79. [CrossRef]
41. Fan, Q.; Li, X.; Yang, Z.; Han, J.; Xu, S.; Zhang, F. Double-Confined Nickel Nanocatalyst Derived from Layered Double Hydroxide Precursor: Atomic Scale Insight into Microstructure Evolution. *Chem. Mater.* **2016**, *28*, 6296–6304. [CrossRef]
42. Chen, H.; He, S.; Cao, X.; Zhang, S.; Xu, M.; Pu, M.; Su, D.; Wei, M.; Evans, D.G.; Duan, X. Ru-Cluster-Modified Ni Surface Defects toward Selective Bond Breaking between C-O and C-C. *Chem. Mater.* **2016**, *28*, 4751–4761. [CrossRef]
43. Li, C.; Chen, Y.; Zhang, S.; Xu, S.; Zhou, J.; Wang, F.; Wei, M.; Evans, D.G.; Duan, X. Ni-In Intermetallic Nanocrystals as Efficient Catalysts toward Unsaturated Aldehydes Hydrogenation. *Chem. Mater.* **2013**, *25*, 3888–3896. [CrossRef]
44. Li, Z.; Bian, L.; Zhu, Q.; Wang, W. Ni-based catalyst derived from Ni/Mg/Al hydrotalcite–like compounds and its activity in the methanation of carbon monoxide. *Kinet. Catal.* **2014**, *55*, 217–223. [CrossRef]
45. Kim, W.Y.; Lee, Y.H.; Park, H.; Choi, Y.H.; Lee, M.H.; Lee, J.S. Coke tolerance of Ni/Al_2O_3 nanosheet catalyst for dry reforming of methane. *Catal. Sci. Technol.* **2016**, *6*, 2060–2064. [CrossRef]
46. He, S.; Li, C.; Chen, H.; Su, D.; Zhang, B.; Cao, X.; Wang, B.; Wei, M.; Evans, D.G.; Duan, X. A Surface Defect-Promoted Ni Nanocatalyst with Simultaneously Enhanced Activity and Stability. *Chem. Mater.* **2013**, *25*, 1040–1046. [CrossRef]
47. Mitchell, R.W.; Lloyd, D.C.; van de Water, L.G.A.; Ellis, P.R.; Metcalfe, K.A.; Sibbald, C.; Davies, L.H.; Enache, D.I.; Kelly, G.J.; Boyes, E.D.; et al. Effect of Pretreatment Method on the Nanostructure and Performance of Supported Co Catalysts in Fischer-Tropsch Synthesis. *ACS Catal.* **2018**, *8*, 8816–8829. [CrossRef]
48. Li, F.; Liu, J.; Evans, D.G.; Duan, X. Stoichiometric synthesis of pure MFe_2O_4 (M = Mg, Co and Ni) spinel ferrites from tailored layered double hydroxide (hydrotalcite–like) precursors. *Chem. Mater.* **2004**, *16*, 1597–1602. [CrossRef]
49. Liu, J.; Li, C.; Wang, F.; He, S.; Chen, H.; Zhao, Y.; Wei, M.; Evans, D.G.; Duan, X. Enhanced low-temperature activity of CO_2 methanation over highly-dispersed Ni/TiO_2 catalyst. *Catal. Sci. Technol.* **2013**, *3*, 2627–2633. [CrossRef]
50. Grosvenor, A.P.; Biesinger, M.C.; Smart, R.S.C.; McIntyre, N.S. New interpretations of XPS spectra of nickel metal and oxides. *Surf. Sci.* **2006**, *600*, 1771–1779. [CrossRef]
51. Zhang, Y.; Qin, Z.; Wang, G.; Zhu, H.; Dong, M.; Li, S.; Wu, Z.; Li, Z.; Wu, Z.; Zhang, J.; et al. Catalytic performance of MnO_x-NiO composite oxide in lean methane combustion at low temperature. *Appl. Catal. B-Enriron.* **2013**, *129*, 172–181. [CrossRef]
52. Biesinger, M.C.; Payne, B.P.; Grosvenor, A.P.; Lau, L.W.M.; Gerson, A.R.; Smart, R.S.C. Resolving surface chemical states in XPS analysis of first row transition metals, oxides and hydroxides: Cr, Mn, Fe, Co and Ni. *Appl. Surf. Sci.* **2011**, *257*, 2717–2730. [CrossRef]

53. Mo, S.; Li, S.; Li, W.; Li, J.; Chen, J.; Chen, Y. Excellent low temperature performance for total benzene oxidation over mesoporous CoMnAl composited oxides from hydrotalcites. *J. Mater. Chem. A* **2016**, *4*, 8113–8122. [CrossRef]
54. Hernández, W.Y.; Centeno, M.A.; Ivanova, S.; Eloy, P.; Gaigneaux, E.M.; Odriozola, J.A. Cu-modified cryptomelane oxide as active catalyst for CO oxidation reactions. *Appl. Catal. B* **2012**, *123–124*, 27–35. [CrossRef]